ChemPubSoc Europe

DOI: 10.1002/slct.201800988

Chemistry SELECT Full Papers

Sustainable Chemistry

Engineered ZnO-TiO_2 Nanospheres for High Performing Membrane Assimilated Photocatalytic Water Remediation and Energy Harvesting

Kiran P. Shejale, Devika Laishram, Ritu Gupta, and Rakesh K. Sharma*[a]

This paper is a study of ZnO doped TiO_2 in various percentages ranging from 0% (undoped) up to 10%. The effect of doping was observed via the change in morphological, optical, electrical and physical properties of ZnO-TiO_2 nanospheres. Hydrothermally grown nanospheres are used for removing contaminants photo-catalytically from waste water and also as photoanodes in dye-sensitized solar cells (DSSCs) with graphene as counter electrode. Of the many approaches that have been explored for purification of contaminated water, this work presents designing of an environmental friendly solution, based on easily available filter paper membrane and incorporating it with the synthesized catalyst for photodegradation of the harmful toxic substances. These reusable membranes assist in the photodegradation process by creating room for better light-catalyst-dye interaction via large surface sites. The spherically structured heterojunction of ZnO-TiO_2 generates excitons that oxidize methyl orange (MO) and reduce harmful Cr(VI) to non-toxic Cr(III) with high efficacy. Additionally, the agile nanostructures were employed as efficient photoanode material by fabricating dye sensitized solar cells with graphene as counter electrode.

Introduction

According to the World Health Organization, 844 million people suffer from lack of basic drinking water service and 159 million people depend on surface water. It has been estimated that by the year 2025, one-half of the total population in the world will be living in the water-stressed areas. Apart from these, contaminated water transmits many diseases leading to death.[1] Thus, effectively addressing the water shortage of an exponentially rising population without damaging the environment in any way is a major concern today. Contaminants in the form of organic and inorganic waste discharge give rise to shortage of potable water and various other crisis.[2,3] The major contributor includes waste from industries such as dyes used in leather tanning, textile, paints, electroplating, etc. that generate potential carcinogens and non-biodegradable by-product.[4] Another potentially lethal pollutant is heavy metal pollutants such as Cr(VI), harming terrestrial and aquatic life systems mainly caused by mining, ore processing and chemical manufacturing industries.[5,6] One constructive way to fight against the water-related stress is re-using water by means of several purification techniques.[7] Decontamination and regeneration of water via solar energy has emerged as a preferred method among the clean and sustainable form of purifying polluted water.[8-11] A photocatalytic material is used for the process of decontamination and purification whereby it absorbs sunlight at a specific wavelength creating active species that react with the contaminants resulting in the production of non-toxic output.[10,12] In addition to this, recently, photo-thermal water evaporation with plasmonic interfacial system are used that increases confined heating process. Merging solar evaporation with photocatalytic reactions, Liu *et al.* fabricated bi-functional membranes of TiO_2, Au nanoparticle on anodized aluminum oxide that showed significant decontamination efficiency.[7] Li *et al* also assembled chitosan/polycaprolactum filter paper and tested it for reduction of Cr(VI) to Cr(III).[13] However, these processes mainly include high-cost metal nanoparticles, acidic conditions and sophisticated equipment which make them less viable option for large and continuous usage. Additionally, adsorption and reduction are commonly adopted for removing toxic Cr(VI) pollutants from surface and groundwater as these strategies offers higher efficiency at low cost without any negative by-products.[14] Nevertheless, semiconductor based photocatalytic degradation is adopted as a preferred method for removing pernicious waste from water as it offers regeneration and reusability by reducing harmful substances without alleviating the toxicity. Some of the commonly used forms of semiconductor include – (i) plasmonic metal nanoparticle such as Ag and Au based multifunctional semiconductor heterostructure[15] (ii) carbon as co-catalyst in organic-inorganic hybrid nanocomposite[16] (iii) semiconductor/metal oxide nanoparticle[17] and (iv) doping in metal oxide nanoparticle.[18] Among these, metal oxide semiconductors offer properties such as appropriate band gap, flat band potential, low cost, abundance, low electrical resistance, good scalability and stability. And hence, these materials are expediently utilized in applications like photo electrochemical

[a] *K. P. Shejale, D. Laishram, R. Gupta, R. K. Sharma*
Department of Chemistry, Indian Institute of Technology Jodhpur, NH 65, Karwar, Jodhpur, Rajasthan, India, 342037
Tel.: +91 291 280 1303
E-mail: rks@iitj.ac.in

Supporting information for this article is available on the WWW under https://doi.org/10.1002/slct.201800988

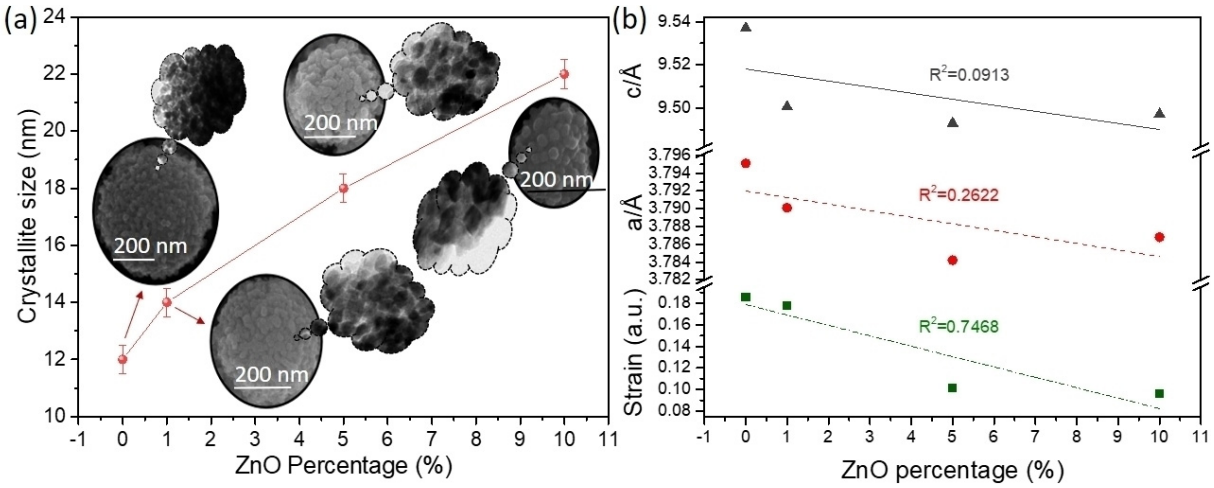

Figure 1. (a) Effect of ZnO doping percentage on crystallite size and morphology and (b) Cell parameters and lattice strain on ZnO % variation.

(PEC) cells for renewable energy based applications. Amid all the semiconductors used, TiO_2 is ubiquitously utilized because of its low cost, non-toxicity and stability. However, TiO_2 suffers from certain disadvantages like fast charge recombination and limited UV absorption. To augment certain inadequacies and also to harness its full potential, doping is performed with another semiconductor nanomaterial, ZnO, which displays high mobility of electrons.[19-21] In our previous work, the composite of ZnO and TiO_2 was demonstrated to exhibit effective surface charge trapping with increased charge isolation as they have matching band energy levels thereby creating a perfect heterojunction with photo induced electrons enrichment in ZnO and holes in TiO_2.[22-25] This lead to decrease recombination of charge exciton pairs consequently increasing the lifetime and efficiency of dye sensitized solar cell. The surge of the available surface charge of ZnO-TiO_2 can also result in it being an efficient photocatalyst ultimately improving the redox activity.[26,27] The combination of TiO_2 and ZnO with superior property and PEC activity is well documented in literature reports for applications including DSSC (dye sensitized solar cells)[19,28] and PEC based photocatalysis.[29,30]

In this present study, a facile and environmental friendly membrane loaded with the ZnO-TiO_2 nanospheres has been designed by a filtration process to maximize the photo-degradation of water contaminants. A hydrothermal method was adopted for the synthesis of ZnO-TiO_2 heterojunction nanospheres with high surface area with good light scattering ability.[31] The ZnO doping up on TiO_2 in various percentages has been carried out by varying the concentration of dopant (i.e. ZnO). The synthesized material have been consequently used for applications like dye degradation and DSSC, to fully understand and explore the properties of ZnO-TiO_2 hetero-structure. Heterogeneous catalyst has been earlier reported in the literature to have property for remediation of waste water pollutants.[32,33] This study, however, aims at using the ZnO-TiO_2 nanosphere as a potential candidate in a nanoparticle-assisted membrane-based purification process for degrading water contaminants significantly. The membrane having porous structure along with the nano-spherical heterojunction photo-catalyst traps lights better alleviating the degradation efficiency of harmful contaminants such as methyl orange (MO) and Cr(VI). The heterojunction between the two semiconductor nanomaterials create an n-type doping effect leading to an enhanced number of available electrons thereby amplifying the degradation effect. Furthermore, these synthesized nano-spheres are examined as a photoanode material during DSSC fabrication using graphene as a counter electrode material.

Results and Discussion

The textural change of doping different percentages (0, 1, 5 and 10 %) of ZnO up on TiO_2 sphere is shown in Figure 1a. All the diffraction peaks are indexed to the anatase phase of TiO_2 according to JCPDS No. 21-1272. Scherrer equation was used for estimating the crystallite size from the highest intense (101) X-ray diffraction peak (see Figure S2, Supporting Information and summarized in Table 1). The XRD pattern became sharp and narrow with increasing ZnO percentage and thus the resultant crystallite size followed a linearly increasing pattern (12 to 22 nm). This result is in agreement with the FESEM images in Figure 1a, where the nanoparticles comprising the spheres increases in size with doping percentage. Rietveld Analysis of the X-ray diffraction pattern of all the synthesized samples were carried out to determine the structural changes due to ZnO doping as shown in Figure 1b. The calculated profile factor (Rp), weight profile factor (Rwp) and the goodness of fit (S) together increases on crystallite size as indicated in Table 1. Additionally, the lattice cell parameters showed infin-itesimal change as a function of ZnO doping, e.g., *a* (3.7973 to 3.7914 Å) and *c* (9.5154 to 9.512 Å) on increasing doping % from 0 to 10%. Such influence on the structural parameters can be an indication of the formation of heterojunction in the synthesized nanospheres.[34,35]

Table 1. Crystallite parameters of the various ZnO-TiO_2 nanosphere.[a]

ZnO %	Wt. % of Zn	a (Å)	c (Å)	R_p (%)	R_{wp} (%)	S	Lattice strain (a.u.)	Average crystallite size (nm)
0	0	3.7951	9.5370	8.19	11.8	1.1348	0.1855	12
1	0.45	3.7901	9.5006	5.07	6.23	1.8968	0.1775	14
5	1.81	3.7842	9.4930	5.17	6.44	1.7490	0.1013	18
10	3.09	3.7868	9.4972	5.09	6.33	1.9914	0.0962	22

[a]a and c are the lattice parameters. R_p, R_{wp} and S are the profile factor, weight profile factor, the goodness of fit, respectively.

To support these finding, the lattice strain for all the synthesized nanomaterial were calculated by Williamson–Hall plot[36] as shown in Figure S3, Supporting Information and summarized in Table 1. As indicated in Figure 1b, the lattice strain was reduced from 0.1855 to 0.0962 a.u. on varying ZnO from 0 to 10%. The strain variation between 0 to 1% ZnO (5%) was observed to be very small compared to 0 to 10% ZnO (48%). The defects in the grain boundaries effectively enhances the strain in the lattice and crystallite size indicating reduced crystallite size over lower ZnO percentage. This is in agreement with average crystallite trend as shown in Table 1. The decrease in strain with increase in doping concentration is likely due to the filling of the Ti interstitial atoms by Zn leading to a compressive strain on the lattice of TiO_2 in the high percentage doped TiO_2 spheres. Moreover, the increase in doping concentration leads to more number of Zn atoms diffusing in the TiO_2 dislocation sites thereby increasing the crystallite size and reducing the strain.[37,38]

The surface area of the prepared ZnO-TiO_2 nanospheres were estimated by means of Brunauer Emmett Teller (BET) adsorption-desorption isotherm curves (see Figure S4, Supporting Information). The observed isotherm conforms to type IV having H3 type hysteresis loop indicating the existence of lamella like pore structure as discussed in previous study.[31] The highest surface area was observed at 1% ZnO doped TiO_2 having a value of 95.23 m^2/g and gradually decreases up to ~ 51% for 10% ZnO-TiO_2. Similar observations were made for the pore size distribution and pore volume. The amount of ZnO doping percentages thus played a crucial role in shaping the crystallite size, specific surface area and pore size distribution.

The band gap (E_g) of the samples were calculated from equation $(\alpha h\nu)^{1/2} = A^{1/2}(h\nu - E_g)$ using the Tauc method[39] as shown in Figure 2a and summarized in Table 2. Theoretical calculations and experimental results show that ZnO and TiO_2 nanospheres have a direct forbidden optical band gap.[8] In case of ZnO doping in TiO_2, red shift was observed with higher ZnO %. This overall shift is less and in accordance with actual Zn doping concentration (3.09%, atomic). The observed red shift can be attributed to E_g of anatase TiO_2 and ZnO, ~ 3.2 and 3.3 respectively, which results in the blue shifting of the overall band gap of type II heterojunction ZnO-TiO_2 sphere. Moreover, uniform distribution of ZnO within the sphere, surface area and defects have a prominent contribution in the bandgap shifting.

The flat band potential (E_{fb}) determines the donor density (N_d) and band edge positions from the Mott-Schottky (M-S) plot[40] as shown in Figure 2b by explicitly exploring the conduction band electrons and valance band hole energies at

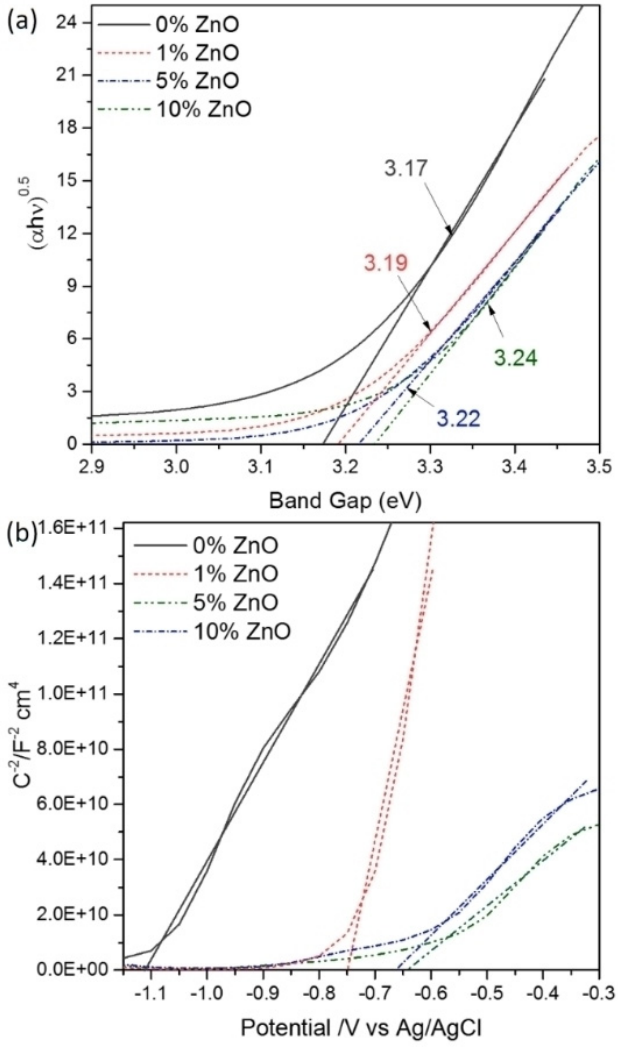

Figure 2. (a) Tauc and (b) Mott-Schottky plots for various ZnO-TiO_2.

Table 2. Band gap, flat band potential (E_{fb}) and donor density (N_d) of ZnO-TiO_2 nanosphere with different ZnO doping.

ZnO %	Band Gap (eV)	E_{fb}/V vs Ag/AgCl	Donor density ($N_d \times 10^{17}$ cm^{-3})
0	3.17	-0.63	1.53
1	3.19	-0.66	7.29
5	3.22	-0.75	8.84
10	3.24	-1.11	4.11

semiconductor-electrolyte interface.[41] The E_{fb} and N_d of all the different percentage doped ZnO-TiO_2 films were calculated from M-S plot as shown in Figure 2b using the equation $1/C^2 = (2/q\varepsilon_0 N_d)(E - E_{fb} - KT/q)$, where C is the capacitance of the space layer, q is the elementary electron charge, ε is the dielectric constant of the ZnO-TiO_2 layer, ε_0 is the vacuum permittivity, N_d is the donor density, E is the applied potential, E_{fb} is the flat band applied potential, K is the Boltzmann constant and T is the absolute temperature. The curves are in concordance with n-type semiconductor behavior where the donor density is associated with electrons. As summarized in Table 2, the E_{fb} is shifted to more positive value (~76%) with increase in Zn doping concentration from 0 to 10%. This indicates the shifting of fermi level of ZnO-TiO_2 towards conduction band on increasing doping percentage. Similar observations were made in Tauc plot (Figure 2a). The donor densities calculated from the slope of M-S plots is shown in Table 2. When Zn percentage is increased from 0 to 1%, N_d or number of electrons were increased from 1.53 to 7.29×10^{17} cm^{-3} which can be attributed to high surface area (95.23 m^2/g) due to Zn incorporation (1%) in TiO_2. Thus, the highly porous type II heterojunction ZnO-TiO_2 structure can be attributed to higher charge carrier density. However, at 5% and 10% Zn doping, donor density firstly increased and reduced subsequently. This data agrees well with previous characterization of TEM images BET surface area and XRD findings. Thus, at higher Zn doping % high crystallinity and low surface area could lead to lower donor densities.

Figure 3 shows the morphological analysis of the ZnO-TiO_2 nanospheres. It was found that all the samples with variable ZnO% were in solid spherical shape with uniform nature as precursor beads and sphere (see Figure S5a and b, Supporting Information). Interestingly, the average diameter of the sphere is reduced when the ZnO doping percentage was changed from 0% to 10% (see Figure 3a-d). It can be observed that the surface of the solid sphere is rough and possesses high-density pores and larger crystallite size with ZnO doping % which is in accordance with the XRD findings. The selected area electron diffraction pattern of the 5% ZnO-TiO_2 reveals polycrystalline diffraction rings that corresponds to the anatase phase of TiO_2. The lower concentration of ZnO could be the reason behind the absence of ZnO diffraction ring as shown in left part of Figure S5c, Supporting Information. The HRTEM image revealed lattice fringes of TiO_2 and ZnO having interplanar spacing calculated to be 0.35nm corresponding to the (101) plane of anatase TiO_2 and 0.26nm for the (002) plane for wurtzite phase of ZnO. The elemental mapping revealed that Ti K, Zn K and O K were uniformly distributed all over the ZnO-TiO_2 sphere (See Figure S5d, Supporting Information).

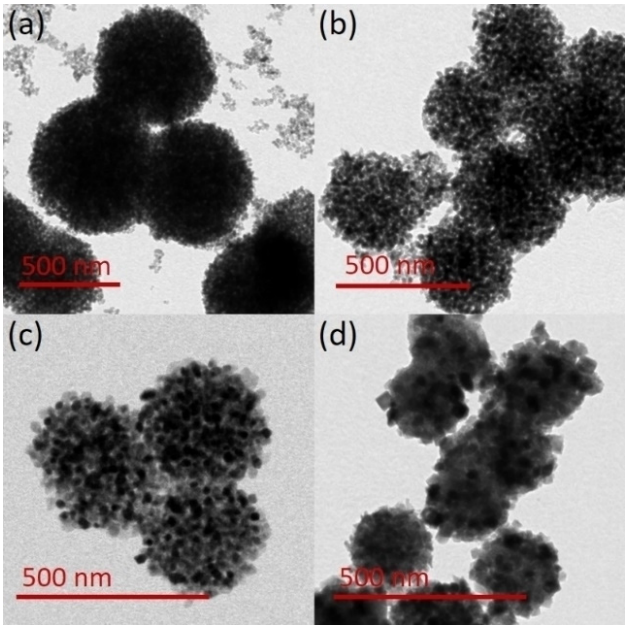

Figure 3. (a-d) TEM images of 0, 1, 5 and 10 % ZnO-TiO_2 respectively.

In order to understand the chemical state and to confirm the presence of the ZnO, all samples were investigated by XPS. The XPS survey spectra of 0%, 1%, 5% and 10% ZnO-TiO_2 is shown in Figure S6, Supporting Information, where the intensities of the Ti 2p, Zn 2p and O 1s were increased with the enhancing percentage of ZnO in the TiO_2 sphere.[31]

Figure 4(a-d) shows high resolution Ti 2p XPS spectra of the ZnO-TiO_2 sphere with different ZnO doping. In all the Ti 2p spectra, the two main peaks of Ti $2p^{3/2}$ and Ti $2p^{1/2}$ are situated at binding energies 458 and 464 eV respectively due to spin-orbit splitting and corresponds to titanium dioxide (Ti^{4+}).[40,42] Apart from these peaks at 458.6 and 464.4 eV, 0% ZnO showed one more shoulder peak of Ti^{3+} at binding energy 456.9 eV which consists of Ti_2O_3 as shown in Figure 4a. This confirms the formation of both TiO_2 and Ti_2O_3 in the sample. After doping with 1% ZnO, the Ti $2p^{3/2}$ and Ti $2p^{1/2}$ peaks position were similar to 0%, but Ti^{3+} peak shows a slight shift in the position at 457.1 eV and variation in all peak areas (Figure 4a). The shift in the peak position can be attributed to the few Ti atoms that were substituted by Zn resulting in a change in the electronic state of Ti. Compared to 0%, the peak area of the Ti^{4+} and Ti^{3+} in 1% doped TiO_2 is increased by 12 and 13% respectively. The increase in Ti^{4+} indicates an enhancement in the TiO_2 structure whereas in case of Ti^{3+} it shows the formation of other metal oxide. However, for 5% and 10% ZnO, Ti 2p spectra fitted with only two peaks attributing to Ti^{4+} as 458.4 and 464.2 eV as shown in the Figure 4c and 4d. The Ti^{3+} peak clearly disappears on doping with higher percentage of ZnO as expected due to the formation of Ti-O-Zn structure in TiO_2 lattice.[43] The variation in the area of the peaks were directly estimated by the stoichiometry change. The peak for Ti^{4+} maximum increased by 25% on higher ZnO doping.

The high resolution spectra of O 1s of 0% ZnO is shown in Figure 4e with three deconvoluted peaks at binding energies 528.1, 530 and 530.8 eV which refers to the dissociated or non-lattice oxygen/OH (O_C), lattice oxygen in O_2^- form (O_L) and vacancies/defects (O_V).[44,45] Similarly, for doping by 1 and 5 % ZnO in TiO_2 sphere, three peaks are fitted with an observed slight red shift as shown in the Figure 4f and 4g. This indicates the presence of metal oxide in TiO_2 on ZnO doping. In the

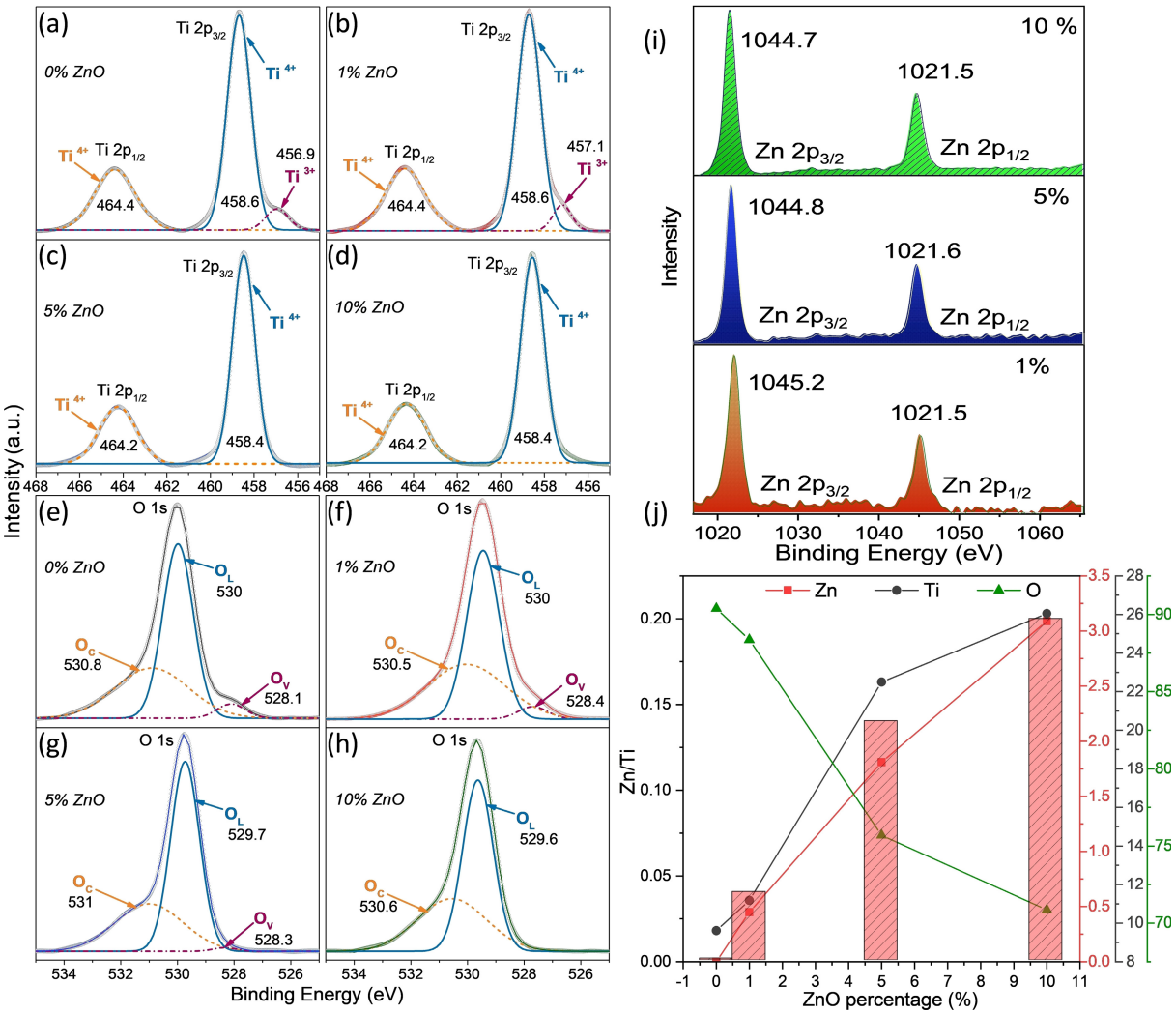

Figure 4. High resolution XPS spectra of (a-d) Ti 2p, (e-h) O 1s of 0, 1, 5 and 10 % ZnO-TiO_2 respectively, (i) Zn 2p of all samples, and (j) Zn/Ti with Zn, Ti and O weight percentage as a function of ZnO percentage in ZnO-TiO_2.

stoichiometry change, as the doping percentage increased from 0 to 5%, the peak area at 530.8 and 530 eV increases by 4 and 11% respectively, while the peak area at 528.1 eV decreases by 84%. For the 10% doping, only two peaks at 529.6 and 530.6 eV were found and designated to lattice and non-lattice oxygen repectively. Furthermore, the peaks attributed to vacancies and defects disappeared. In comparison to 0%, the peak area at 529.6 and 530.6 eV of 10% ZnO-TiO_2 sphere increased by 92% and 6% respectively. This enhancement in the peak area of lattice oxygen is in agreement with the Ti 2p XPS spectra.

The high resolution XPS spectra of Zn 2p shown in Figure 4i and contains two peaks at binding energy 1044 and 1021 eV corresponding to Zn $2p^{3/2}$ and Zn $2p^{1/2}$ repectively. These peaks exhibit a binding energy difference of 23.2 eV and is in agreement with the standard ZnO XPS spectrum.[46,47] At 0% ZnO-TiO_2, the peaks were absent as ZnO percentage is zero, however Zn 2p peaks start appearing at 1% ZnO doping and further increase in its intensity with higher doping percentages takes place for 5% and 10%. Figure 4j summarizes the actual weight percentage of Zn, Ti and O over varying percentage of ZnO from 0 to 10% during ZnO-TiO_2 preparation. The bulk Zn/Ti atomic ratio and individual elemental percentage were analyzed by XPS and electron dispersive spectra respectively (see Figure 4j). The Zn/Ti atomic ratio was 0.04 at 1% and increased up to 0.2 over 10% ZnO, which strongly indicates the random distribution of Zn and Ti elements all over the nanosphere. The Zn percentage enhanced from 0 to 3.09% indicating successful incorporation of ZnO from 0 to 10% respectively, and the mismatch confirms the growth of ZnO-TiO_2 heterojunction (see Figure 4j).

Vacuum filtration is a simple approach for the formation of thin film on porous substrate compared to other conventional methods like spin coating, interfacial and evaporation.[48] Films produced by the vacuum filtration offers wide range of optimization in terms of film thickness, compositions and flexibility. Such process is especially useful for very large scale production with high reproducibility and provides homoge-

neous, layer-by-layer formation along with highly stable structures. The filter paper (Fp) was taken as the preferred paper substrate due to its cost effectiveness, eco-friendly and biodegradable nature. Moreover, high porosity to absorbance leads to coating of more sample on the surface with significant strength to sustain pressure, multiple coatings and washings. The Fp-ZnO-TiO_2 membrane is prepared by a simple process as schematically demonstrated in Figure S1, Supporting Information. The membrane fabrication details are mentioned in the experimental section. Briefly, the solution consisting of ZnO-TiO_2, surfactant and distilled water (1:1x10^{-4}:1) was made to pass through the Fp by using mild vacuum followed by washing with D/W for several times and annealing overnight at 60°C. Interestingly, after the first use, mere washing with DI water and annealing at 60°C, the membrane was made ready to use for the next cycle.

A distinct deposition/layer can be clearly observed after fabricating Fp-ZnO-TiO_2 membrane as shown in Figure 5a. With

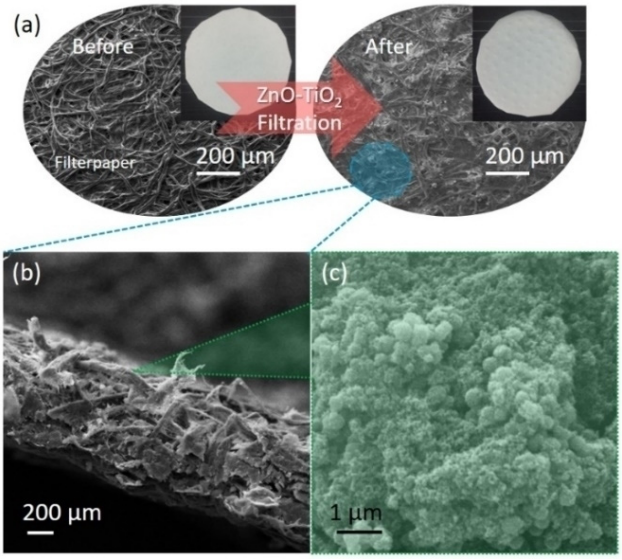

Figure 5. SEM images of Fp (a) before and after ZnO-TiO_2 filtration where inset shows photographs of same, (b) Cross-sectional image and (c) surface morphology of 5% Fp-ZnO-TiO_2 membrane.

uniform distribution, some discrete islands of sphere were formed on the Fp surface (Figure 5a, right). The inset Figure 5a shows the before and after photographs of Fp-ZnO-TiO_2 membrane. It can be seen through Figure 5b that Fp-ZnO-TiO_2 formed a uniform and compact layer (~3 µm) all over the highly porous Fp. The sphere diameter of ZnO-TiO_2 is varying with ZnO percentage from 600 to 200 nm, and way smaller than the membrane pores which eventually resulted in the stable and porous structure. This can be very useful to minimize the loss and reuse of catalyst during water treatment. The vacuum created by suction deposits highly dense, randomly distributed spheres, interpenetrated with moderately aggregated and physically stable film as shown in Figure 5c.

The photodegradation of methyl orange (MO) and Cr(VI) (typical organic pollutant in the textile and leather industries effluents) with 0%, 1%, 5% and 10 % of ZnO-TiO_2 as well as Fp-ZnO-TiO_2 was investigated at pH 6.58, room temperature and under 1 sun irradiation (Figure 6). On an average, the experiments were repeated for 3 times to check repeatability, and the adsorption/desorption equilibrium was obtained by exploring Fp in contaminated water for 1 hour in dark condition. All the photocatalytic process follows the pseudo first order reaction kinetics (see Figure S7, Supporting Information) and apparent rate constant (k min^{-1}) with high coefficient ($R^2 \geq 0.95$). After 120 min of irradiation, the highest degradation was 92% for MO demonstrated by 1% ZnO-TiO_2 as shown in the Figure 6a which is attributed to the specific surface area (95.23 m^2/g) and donor (electron) density (7.29 × 10^{17} cm^{-3}) of type II heterojunction ZnO-TiO_2 structure. The MO removal efficiency followed the chronological order 1% (92%) > 5 (84%) > 10 (81%) > 0 (77%) > blank (55%) agreeing with various structural and physical properties like crystallite size, lattice strain, specific surface area, band gap and donor density. The 0, 1, 5 and 10% Fp-ZnO-TiO_2 showed (Figure 6b) remarkable enhancement in MO removal efficiency in comparison to ZnO-TiO_2. As shown in Figure 6b, the 1% Fp-ZnO-TiO_2 system reports complete MO photodegradation within 80 mins of the start of the reaction. On the other hand, the blank (33%), 0 (54%), 5 (94%) and 10% (90%) Fp-ZnO-TiO_2 showed increased MO photodegradation performance in 120 min. The apparent MO removal rate constants (k) for both ZnO-TiO_2 and Fp-ZnO-TiO_2 were calculated and shown in Figure 6c. It is interesting to note that, in 1% ZnO-TiO_2, the MO photodegradation performance was dramatically enhanced (by ~ 2 times) from 0.0182 to 0.0556 min^{-1} just by the introduction of Fp system in it (1% Fp-ZnO-TiO_2). The Cr(VI) removal efficiency and the rate constant followed the same pattern as observed in the MO removal (see Figure 6d, e). In the event of using Cr(VI) as water contaminant, 95% of Cr (VI) was photodegraded after 180 min into the reaction for 1% ZnO-TiO_2 as shown in Figure 6d. The 1% Fp-ZnO-TiO_2 showed highest Cr(VI) photodegradation efficiency as complete photodegradation of impurities occurred over 160 min (see Figure 6e). With pseudo-first order reaction (Figure S7, Supporting Information), the rate constant of Fp-ZnO-TiO_2 follows the order 0.0223 min^{-1} (1%) > 0.0097 min^{-1} (10%) > 0.008 min^{-1} (5%) > 0.0076 min^{-1} (0%) > 0.0068min^{-1} (blank). Similar to MO, photodegradation of Cr(VI) rate was also increased by ~ 2 times for 1% Fp-ZnO-TiO_2 system and significant enhancement in blank and other ZnO% were also observed as shown in Figure 6f. To support the above finding, the trend between 1 to 5% Fp-ZnO-TiO_2 was also examined where 2% Fp-ZnO-TiO_2 was observed to have 53 and 76% photodegradation of MO and Cr(VI) as water contaminates respectively. Moreover, it followed the same trend as the ZnO doping percentage gets higher as 5 and 10% (see Figure S8a and b, Supporting Information).

The Fp-ZnO-TiO_2 was made to float in the contaminated water pollutant system. The solar thermal heat generated by the solar simulator along with a constant stirring at 150 rpm delocalized the photodegradation in the system completely.[49]

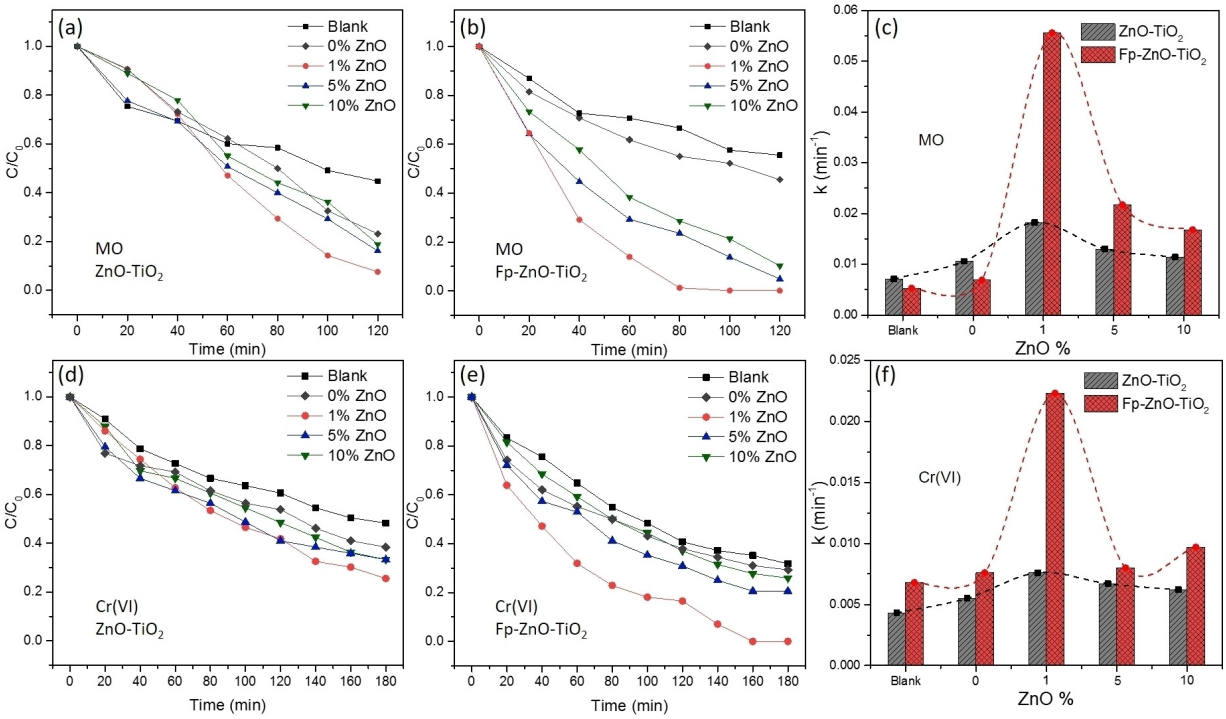

Figure 6. Time profile photocatalytic conversion of (a, d) ZnO-TiO_2 and (b, e) Fp-ZnO-TiO_2 with methyl orange (MO) and Cr(VI) as water contaminant respectively, (c, f) comparison of MO and Cr(VI) photodegradation rate constant *k* over various ZnO % in ZnO-TiO_2 respectively. Blank demonstrates condition without any catalyst. The dotted lines in c and f are guide to eye.

The synergistic enhancement in the photodegradation of the MO and Cr(VI) by Fp-ZnO-TiO_2 system is mainly attributed to two factors and is schematically demonstrated in Figure 7.

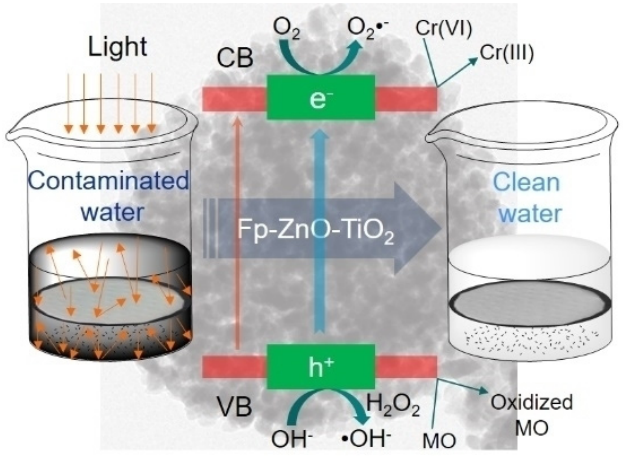

Figure 7. Schematic illustration of the photodegradation of water contaminants like MO and Cr(VI) by Fp-ZnO-TiO_2 under 1 sun irradiation.

Firstly, ZnO-TiO_2 heterojunction exhibits high charge density and provides the essential driving force for charge separation.[7] This superior electron-hole pair generation further have a long-life due to highly dense packed ZnO-TiO_2 nanospherical structure. Moreover, this mesoporous hierarchy has multiple sites for harvesting and scattering light, thus, inducing efficient photodegradation. The ZnO-TiO_2 structure with its band gap > 3.2 eV belonging to the type II heterojunctions generates photo-catalytically active holes at valance band and oxidizes the organic MO whereas the Cr(VI) consumes the electron at conduction band and rapidly gets reduced to non-toxic Cr(III). Structure exhibiting such behaviors efficiently reduces charge recombination and significantly enhances the photodegradation. Secondly, as shown in Figure 7, the floating Fp improves the delocalization of light and results in dramatic increase the light absorbance ability.[31] Altogether, ~1μm thick and highly porous Fp along with ZnO-TiO_2 having high specific area can effectively trap more contaminants causing an efficient photodegradation of water compared to degradation observed by ZnO-TiO_2 alone.

The effect of ZnO-TiO_2 nanosphere specific surface area on the photodegradation ability was also studied and is demonstrated in Figure 8. The normalized specific surface area for MO and Cr(VI) removal and the rate constant k' (g min^{-1} m^{-2}) was calculated by using the equation $k' = k/S_{BET}$, where k (min^{-1}) is the removal rate constant of these contaminants and S_{BET} (g m^{-2}) is the specific surface area of 0%, 1%, 5% and 10 % ZnO-TiO_2 repectively.[5] Blank experiments in Figure 6 suggested that the change in the concentration of water contaminants using Fp without any catalyst (ZnO-TiO_2) and is insignificant compared to the different % of ZnO-TiO_2 and thus it can be attributed to the self-degradation of dye under 1 sun radiation. The MO

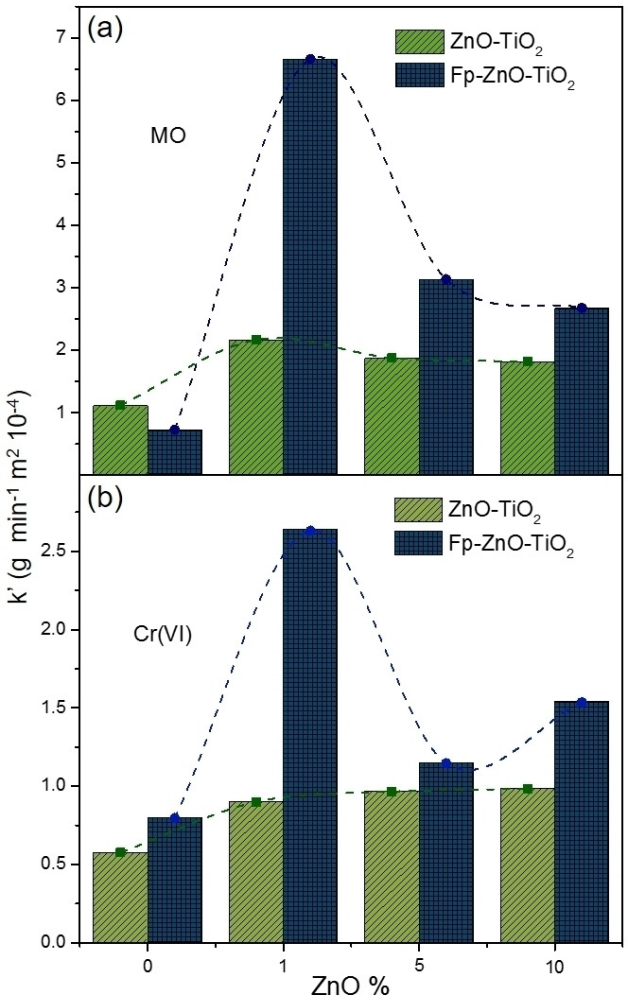

Figure 8. Comparison of normalized specific surface area (a) MO and (b) Cr(VI) photodegradation rate constant *k'* over various ZnO % in ZnO-TiO_2 respectively with and without Fp.

removal performance also (see Figure 8a) followed similar trend while the Cr(VI) removal efficiency showed significant enhancement because of the specific surface area over rate constant as shown in Figure 8b. The Cr(VI) removal rate increased by ~ 2 times for 1% Fp-ZnO-TiO_2 over the normalized specific surface area. Whereas, in case of ZnO-TiO_2, after 1% ZnO, Cr(VI) removal rate is stabilized due to high crystallite size of ZnO-TiO_2 with prolonged irradiation exposure and have marginal potential to increase Cr(VI) decomposition kinetics.

The Fp-ZnO-TiO_2 also showed a good reusability as shown in Figure S9, Supporting Information. After immediate cleaning with D/W and overnight annealing at 60°C, Fp were ready to use for the next cycle. After using for 3 consecutive cycles, photodegradation of MO and Cr(VI) by 1% Fp-ZnO-TiO_2 demonstrated a drop in the removal efficiency by an amount of 5 and 6% respectively. The fabrication of Fp-ZnO-TiO_2 is a simple, eco-friendly and cost-effective process and have a large potential for targeting various other kinds of water contaminants. A comparative literature review of various nanomaterial systems used for degrading different agents of pollution is given in Supporting Information Table S2.

Further, these ZnO-TiO_2 nanosphere were extensive explored as energy harvesting semiconductor metal oxide, The third-generation solar cell, dye sensitized solar cells (DSSC) is simple, fast developing and cost-efficient solar cell which has attracted many attention for energy harvesting.[32] As reported in our recent study, high photoconversion efficiency was achieved by solid ZnO-TiO_2 nanosphere on varying ZnO doping percentage along with the use of Pt as counter electrode.[31] A polydisperse aggregate structure of 1% ZnO-TiO_2 solid nanosphere facilitates high light scattering ability and creates good electron trapping sites. Together with increased number of anchoring sites for dyes and better architecture for electron transport, harvesting of photon has increased with lower recombination rate. As shown in Figure S10 and Table S1 Supporting Information, among all the different doping percentage of ZnO synthesized, 1% doped was reported with highest photo-conversion efficiency and was used to further explore using graphene as counter electrode in this study.

The performance of 1% ZnO-TiO_2 solar cells was reportedly reduced by $\Delta\eta$ ~ 11% on replacing Pt with graphene as active part/catalytic part of the counter electrode (see Figure 9a and performance parameters summarized in Table 3). The highest photo conversion efficiency (8.25%) has been reported with Pt counter electrode whereas with similar composition, 7.3% efficiency was observed using graphene as counter electrode with reduced photocurrent density from 19.39 to 17.30 mA/cm^2 respectively. Graphene, 2d sheets of sp^2 bonded carbon atoms have high conductivity (> 200 000 cm^2 V^{-1} s^{-1}), optical transparency (97.7%) and a high specific surface area (2630 m^2 g^{-1}) most importantly it showed significant chemical stability and catalytic activity, but still does not outperform Pt counter electrode in performance.[50] Traditional Pt counter electrode has better performance but it implies that about 60% of the total fabrication cost is spent for its sole purpose. So, replacement of Pt with graphene for the counter electrode aspect of DSSC is a viable option even with lesser efficiency.[51]

Table 3. Photovoltaic parameters of 1% ZnO-TiO_2 photoanode DSSC with different counter electrodes (CE).[b]

Active part of CE	Jsc (mA/cm^2)	Voc (V)	FF (%)	η (%)
Pt	19.39	0.7	61	8.25
Graphene	17.30	0.69	62	7.3

[b]Jsc, Voc, FF and η are the short circuit current, open circuit voltage, fill factor and efficiency, respectively. The with 0.04 cm^2 active area, all cells performance measurement were carried out under 1sun irradiation.

Electrochemical impedance spectroscopy technique has been mainly explored to investigate electron transport mechanism in DSSC. The impedance spectra were measured ranging from 0.01 Hz to 100 kHz and shows three well defined semicircles (See Figure 9b). The inset represents the equivalent circuit considering the Warburg diffusion resistance at the oxide-electrolyte interface and electron diffusion at counter

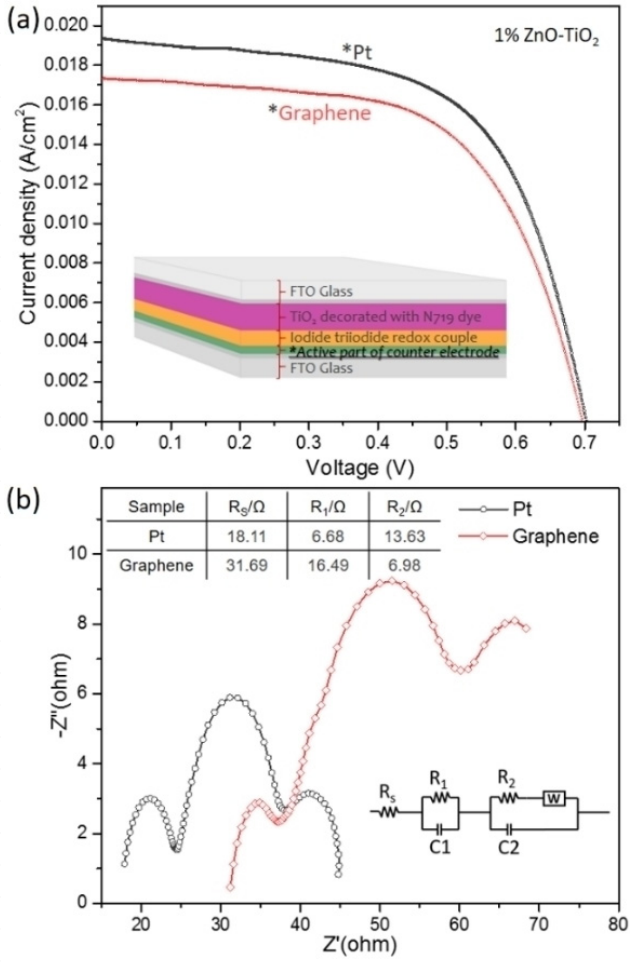

Figure 9. (a) Current density-voltage curves of the DSSC fabricated using 1% ZnO-TiO_2 as photoanode with Pt and graphene as counter electrodes and (b) Nyquist plots and equivalent circuit (inset) of same with summarized parameters in inset table.

electrode. The first semicircle in Nyquist plots is ascribed to the sheet resistance (R_s) at the interfaces of FTO and the contacts. The second semicircle is fitted to charge transfer resistance (R_1) at redox electrolyte and counter electrode.[52,53] In case of graphene as counter electrode material in the fabricated DSSC, R_s and R_1 increased to 31.69 and 16.49 Ω compared to Pt electrode with resistances 18.11 and 6.68/Ω respectively. The charge transfer resistance in case of graphene was marginally enhanced compared to Pt, however graphene based DSSC showed high FF (62%). The graphene based DSSC was reported to have 11% less photoconversion efficiency, compared to the Pt counterpart ($\eta = 8.25$) which is remarkably good taking into account the various facts like cost effectiveness, potential for large scale, flexible solar cell and many more.

Conclusion

In summary, photo catalytic ZnO-TiO_2 heterojunction nanosphere filter paper membrane with different doping percentage was prepared and explored as an efficient water purification system. 1% ZnO-TiO_2 was observed as the most efficient photocatalytic material amongst all the synthesized nanomaterials. Moreover, by comparing two different methods of removing toxic Cr(VI) waste and MO dye, it can be concluded that using filter paper assimilated with ZnO-TiO_2 enormously reduces (by 33% and 11% respectively) the time taken to completely remove the toxic wastes than the conventional dispersion method. This is attributed to good trapping of contaminants increasing the photodegradation effectively. Additionally, use of the nanospheres as photoanode material in DSSC revealed high photoconversion efficiency of 7.23% with graphene as counter electrode which is attributed to the better light harvesting and scattering combined with increased number of trapping sites created due to doping. This work establishes a definite amount of ZnO doping level to be introduced to TiO_2 for efficient use in photodegradation and photoconversion processes. Furthermore, a highly beneficial method of using inexpensive filter paper to effectively reduce toxic waste in minimal amount of time along with high reusability has been proposed.

Supporting Information Summary

Schematic illustration of highly porous ZnO-TiO_2 coated paper fabrication; XRD pattern and Williamson Hall plot of ZnO-TiO_2 with different ZnO doping; nitrogen adsorption-desorption BET surface area; HRTEM and SAED pattern of 5% ZnO-TiO_2 along with Ti K, Zn K and O K elements of same; XPS survey spectra of with different percentage of ZnO; reaction kinetics of all ZnO-TiO_2 and Fp- ZnO-TiO_2 with MO and Cr(VI) as water contaminant respectively; photodegradation of MO and Cr(VI) as water contaminant respectively with 2% Fp-ZnO-TiO_2; repeated photodegradation of water contaminant as 1% Fp-ZnO-TiO_2 for 3 cycles; J-V characteristics of ZnO-TiO_2 sphere as photoanode with various percentage of ZnO; Photovoltaic performance parameters of ZnO-TiO_2 DSSC by varying ZnO doping levels with Pt as counter electrode; Comparative literature review of various nanomaterials used for degradation of different polluting agents

Acknowledgment

The authors would like to thank Indo-UK NERC Water Quality Project DST/TM/INDO-UK/2K17/52 for financial support. We thank the Material Research Centre, MNIT Jaipur, India for providing XPS and TEM facility.

Conflict of Interest

The authors declare no conflict of interest.

Keywords: Hydrothermal synthesis · water contaminants · Cr (VI) · photocatalysis · graphene counter electrode

[1] Drinking-water. http://www.who.int/mediacentre/factsheets/fs391/en/ (02/10/2017).
[2] S. Malato, P. Fernandez-Ibanez, M. I. Maldonado, J. Blanco, W. Gernjak, Decontamination and Disinfection of Water by Solar Photocatalysis: Recent Overview and Trends. *Catal. Today* **2009**, *147*, 1-59.
[3] M. A. Shannon, P. W. Bohn, M. Elimelech, J. G. Georgiadis, B. J. Marinas, A. M. Mayes, Science and Technology for Water Purification in the Coming Decades. *Nature* **2008**, *452*, 301-310.
[4] M. Stylidi, D. I. Kondarides, X. E. Verykios, Visible Light-Induced Photocatalytic Degradation of Acid Orange 7 in Aqueous TiO_2 Suspensions. *Appl. Catal., B* **2004**, *47*, 189.
[5] Y. Mu, Z. Ai, L. Zhang, F. Song, Insight into Core–Shell Dependent Anoxic Cr(VI) Removal with Fe@Fe_2O_3 Nanowires: Indispensable Role of Surface Bound Fe(II). *ACS Applied Materials & Interfaces* **2015**, *7*, (3), 1997-2005.
[6] Y. In-Ho, B. Sunbaek, C. S. Jin, K. W. Kim, Effects of pH and Dissolved Oxygen on Cr(VI) Removal in Fe(0)/H_2O Systems. *J. Hazard. Mater.* **2011**, *186*, 855 – 862.
[7] Y. Liu, J. Lou, M. Ni, C. Song, J. Wu, N. P. Dasgupta, P. Tao, W. Shang, T. Deng, Bioinspired Bifunctional Membrane for Efficient Clean Water Generation. *ACS Applied Materials & Interfaces* **2016**, *8*, (1), 772-779.
[8] A. Mills, R. H. Davies, D. Worsley, Water Purification by Semiconductor Photocatalysis. *Chem. Soc. Rev.* **1993**, *22*, 417 – 425.
[9] S. Dong, J. Feng, M. Fan, Y. Pi, L. Hu, X. Han, M. Liu, J. Sun, J. Sun, Recent Developments in Heterogeneous Photocatalytic Water Treatment Using Visible Light-Responsive Photocatalysts: a Review. *RSC Adv.* **2015**, *5*, 14610 – 14630.
[10] T. Sugita, M. Mori, A. Mase, S. N. Noguchi, T. Tokutome, K. Fujii, C. Hara, K. Katayama, S. Iwamoto, H. Itabashi, Evaluation of the Water-treatment Ability of Silica-doped Titanium Dioxide Coated Glass Plates Using a Cationic Coupling Reagent Based on a Flow Analytical System. *Anal. Sci.* **2015**, *31*, 15 – 21.
[11] Y. Fan, W. Ma, D. Han, S. Gan, X. Dong, L. Niu, Convenient Recycling of 3D AgX/Graphene Aerogels (X = Br, Cl) for Efficient Photocatalytic Degradation of Water Pollutants. *Adv. Mater.* **2015**, *27*, 3767 – 3773.
[12] T. Papadama, N. P. Xekoukoulotakis, I. Poulios, D. Mantzavinos, Photocatalytic Transformation of Acid Orange 20 and Cr(VI) in Aqueous TiO_2 Suspensions. *Journal of Photochemistry and Photobiology A: Chemistry* **2007**, *186*, 308 – 315.
[13] Z. Li, T. Li, L. An, H. Liu, L. Gu, Z. Zhang, Preparation of Chitosan/Polycaprolactamnano Fibrous Filter Paper and its Greatly Enhanced Chromium(VI) Adsorption. *Colloids and Surfaces A: Physicochemical and Engineering Aspects* **2016**, *494*, 65-73.
[14] M. R. Awual, M. M. Hasan, A. Shahat, M. Naushad, H. Shiwaku, T. Yaita, Investigation of Ligand Immobilized Nano-Composite Adsorbent for Efficient Cerium(III) Detection and Recovery. *Chem. Eng. J.* **2015**, *265*, 210–218.
[15] E. Kowalska, K. Yoshiiri, Z. Wei, S. Zheng, E. Kastl, H. Remita, B. Ohtani, S. Rau, Hybrid Photocatalysts Composed of Titania Modified with Plasmonic Nanoparticles and Ruthenium Complexes for Decomposition of Organic Compounds. *Appl. Catal. B* **2015**, *178*, 133-143.
[16] R. Leary, A. Westwood, Carbonaceous Nanomaterials for the Enhancement of TiO_2 Photocatalysis. *Carbon* **2011**, *49*, 741-772.
[17] M. Logar, I. Bračko, A. Potočnik§, B. Jančar, Cu and CuO/Titanate Nanobelt Based Network Assemblies for Enhanced Visible Light Photocatalysis. *Langmuir* **2014**, *30*, (16), 4852–4862.
[18] Y. Zhang, C. Han, M. N. Nadagouda, D. D. Dionysiou, The Fabrication ff Innovative Single Crystal N, F-Codoped Titanium Dioxide Nanowires with Enhanced Photocatalytic Activity for Degradation of Atrazine. *Appl. Catal. B* **2015**, *168–169*, 550-558.
[19] Gonzalez-I. Valls, Lira-Cantu, M., Vertically-aligned Nanostructures of ZnO For Excitonic Solar Cells: A Review. *Energy & Environmental Science* **2009**, *2*, (1), 19-34.
[20] Q. Zhang, C. S. Dandeneau, X. Zhou, G. Cao, ZnO Nanostructures for Dye-Sensitized Solar Cells. *Advanced Materials* **2009**, *21*, (41), 4087-4108.
[21] J. A. Anta, E. Guillén, R. Tena-Zaera, ZnO-Based Dye-Sensitized Solar Cells. *The Journal of Physical Chemistry C* **2012**, *116*, (21), 11413-11425.
[22] T. G. Ulusoy, A. Ghobadi, A. K. Okyay, Surface Engineered Angstrom Thick ZnO-Sheathed TiO_2 Nanowires as Photoanodes for Performance Enhanced Dye-Sensitized Solar Cells. *J. Mater. Chem. A* **2014**, *2*, (40), 16867-16876.
[23] R. Wang, H. Tan, Z. Zhao, G. Zhang, L. Song, W. Dong, Z. Sun, Stable ZnO@TiO_2 Core/Shell Nanorod Arrays with Exposed High Energy Facets for Self-Cleaning Coatings with Anti-Reflective Properties. *J. Mater. Chem. A* **2014**, *2*, (20), 7313-7318.
[24] S. Panigrahi, D. Basak, Core–shell TiO_2@ ZnO Nanorods for Efficient Ultraviolet Photodetection. *Nanoscale* **2011**, *3*, 2336-2341.
[25] S. Mridha, M. Nandi, A. Bhaumik, D. Basak, A Novel and Simple Approach to Enhance Ultraviolet Photosensitivity: Activated-Carbon-Assisted Growth of ZnO Nanoparticles. *Nanotechnology* **2008**, *19*, 27, 275705.
[26] M. Mahanti, T. Ghosha, D. Basak, Enhanced Near Band Edge Luminescence of Ti/ZnO Nanorod Heterostructures due to the Surface Diffusion of Ti. *Nanoscale* **2011**, *3*, 4427-4433.
[27] S. Sarkara, D. Basak, One-step Nano-Engineering of Dispersed Ag–ZnO Nanoparticles' Hybrid in Reduced Graphene Oxide Matrix and its Superior Photocatalytic Property. *CrystEngComm* **2013**,*15*, 7606-7614.
[28] F. Huang, Q. Li, G. J. Thorogood, Cheng, Y.-B.; R. A. Caruso, Zn-doped TiO_2 Electrodes in Dye-Sensitized Solar Cells for Enhanced Photocurrent. *Journal of Materials Chemistry* **2012**, *22*, (33), 17128.
[29] S. Hernandez, V. Cauda, A. Chiodoni, S. Dallorto, A. Sacco, D. Hidalgo, E. Celasco, C. F. Pirri, Optimization of 1D ZnO@TiO_2 Core-Shell Nanostructures for Enhanced Photoelectrochemical Water Splitting Under Solar Light Illumination. *ACS Appl Mater Interfaces* **2014**, *6*, (15), 12153-67.
[30] L. Pan, G.-Q. Shen, J.-W. Zhang, X.-C. Wei, L. Wang, J.-J. Zou, X. Zhang, TiO_2–ZnO Composite Sphere Decorated with ZnO Clusters for Effective Charge Isolation in Photocatalysis. *Industrial & Engineering Chemistry Research* **2015**, *54*, (29), 7226-7232.
[31] K. P. Shejale, D. Laishram, R. Gupta, R. K. Sharma, Zinc Oxide-Titania Heterojunction-based Solid Nanospheres as Photoanodes for Electron-Trapping in Dye-Sensitized Solar Cells. *Energy Technology* **2016**, *5*, 1-7.
[32] L. Junqi, W. Defang, L. Hui, H. Zuoli, Z. Zhenfeng, Synthesis of fluorinated TiO_2 hollow microspheres and their photocatalytic activity under visible light. *Applied Surface Science* **2011**, *257*, (13), 5879-5884.
[33] Y. Yang, G. Wang, Q. Deng, D. H. Ng, H. Zhao, Microwave-assisted Fabrication of Nanoparticulate TiO(2) Microspheres for Synergistic Photocatalytic Removal of Cr(VI) and Methyl Orange. *ACS Appl Mater Interfaces* **2014**, *6*, (4), 3008-15.
[34] Y. Duan, N. Fu, Q. Liu, Y. Fang, X. Zhou, J. Zhang, Y. Lin, Sn-Doped TiO_2 Photoanode for Dye-Sensitized Solar Cells. *The Journal of Physical Chemistry C* **2012**, *116*, (16), 8888-8893.
[35] A. R. M. Dalod, O. G. Grendal, S. L. Skjærvø, K. Inzani, S. M. Selbach, L. Henriksen, W. van Beek, T. Grande, M.-A. Einarsrud, Controlling Oriented Attachment and in Situ Functionalization of TiO_2 Nanoparticles During Hydrothermal Synthesis with APTES. *The Journal of Physical Chemistry C* **2017**, *121*, (21), 11897-11906.
[36] A. Weibel, R. Bouchet, F. Boulc, P. Knauth, The Big Problem of Small Particles: A Comparison of Methods for Determination of Particle Size in Nanocrystalline Anatase Powders. *Chemistry of Materials* **2005**, *17*, (9), 2378-2385.
[37] J. Tauc, R. Grigorovici, A. Vancu, Optical Properties and Electronic Structure of Amorphous Germanium. *physica status solidi (b)* **1966**, *15*, (2), 627-637.
[38] H. Lin, C. P. Huang, W. Li, C. Ni, S. I. Shah, Tseng, Y.-H., Size Dependency of Nanocrystalline TiO_2 on its Optical Property and Photocatalytic Reactivity Exemplified by 2-Chlorophenol. *Applied Catalysis B: Environmental* **2006**, *68*, (1), 1-11.
[39] J. Y. Yang, W. S. Li, H. Li, Y. Sun, R. F. Dou, C. M. Xiong, L. He, J. C. Nie, Grain Size Dependence of Electrical and Optical Properties in Nb-Doped Anatase TiO_2. *Applied Physics Letters* **2009**, *95*, (21), 213105.
[40] M. Radecka, M. Rekas, A. Trenczek-Zajac, K. Zakrzewska, Importance of the band gap energy and flat band potential for application of modified TiO_2 photoanodes in water photolysis. *Journal of Power Sources* **2008**, *181*, (1), 46-55.
[41] S. Hernández; V. Cauda, A. Chiodoni, S. Dallorto, A. Sacco, D. Hidalgo, E. Celasco, C. F. Pirri, Optimization of 1D ZnO@TiO_2 Core–Shell Nanostructures for Enhanced Photoelectrochemical Water Splitting under Solar Light Illumination. *ACS Applied Materials & Interfaces* **2014**, *6*, (15), 12153-12167.
[42] B. Bharti, S. Kumar, H.-N. Lee, R. Kumar, Formation of oxygen vacancies and Ti^{3+} state in TiO_2 thin film and enhanced optical properties by air plasma treatment. *Scientific Reports* **2016**, *6*, 32355.

[43] E. Wang, W. Yang, Y. Cao, Unique Surface Chemical Species on Indium Doped TiO_2 and Their Effect on the Visible Light Photocatalytic Activity. *The Journal of Physical Chemistry C* **2009**, *113*, (49), 20912-20917.
[44] P. T. Hsieh, Y. C. Chen, K. S. Kao, C. M. Wang, Luminescence Mechanism of ZnO Thin Film Investigated by XPS Measurement. *Applied Physics A* **2008**, *90*, (2), 317-321.
[45] N. Xu, L. Liu, X. Sun, X. Liu, D. Han, Y. Wang, R. Han, J. Kang, B. Yu, Characteristics and Mechanism of Conduction/Set Process in TiN/ZnO/Pt Resistance Switching Random-Access Memories. *Applied Physics Letters* **2008**, *92*, (23), 232112.
[46] S. Dutta, S. Chattopadhyay, D. Jana, A. Banerjee, S. Manik, S. K. Pradhan, M. Sutradhar, A. Sarkar, Annealing Effect on Nano-ZnO Powder Studied from Positron Lifetime and Optical Absorption Spectroscopy. *Journal of Applied Physics* **2006**, *100*, (11), 114328.
[47] V. K. Mahajan, M. Misra, K. S. Raja, S. K. Mohapatra, Self-organized TiO_2 Nanotubular Arrays for Photoelectrochemical Hydrogen Generation: Effect of Crystallization and Defect Structures. *Journal of Physics D: Applied Physics* **2008**, *41*, (12), 125307.
[48] B. Guntupalli, P. Liang, J.-H. Lee, Y. Yang, H. Yu, J. Canoura, J. He, W. Li, Y. Weizmann, Y. Xiao, Ambient Filtration Method to Rapidly Prepare Highly Conductive, Paper-Based Porous Gold Films for Electrochemical Biosensing. *ACS Applied Materials & Interfaces* **2015**, *7*, (49), 27049-27058.
[49] Y. Yang, G. Wang, Q. Deng, D. H. L. Ng, H. Zhao, Microwave-Assisted Fabrication of Nanoparticulate TiO_2 Microspheres for Synergistic Photocatalytic Removal of Cr(VI) and Methyl Orange. *ACS Applied Materials & Interfaces* **2014**, *6*, (4), 3008-3015.
[50] J. D. Roy-Mayhew, D. J. Bozym, C. Punckt, I. A. Aksay, Functionalized Graphene as a Catalytic Counter Electrode in Dye-Sensitized Solar Cells. *ACS Nano* **2010**, *4*, (10), 6203-6211.
[51] H. Wang, Y. H. Hu, Graphene as a Counter Electrode Material for Dye-Sensitized Solar Cells. *Energy & Environmental Science* **2012**, *5*, (8), 8182-8188.
[52] J. Bisquert, I. Mora-Seró, Simulation of Steady-State Characteristics of Dye-Sensitized Solar Cells and the Interpretation of the Diffusion Length. *The Journal of Physical Chemistry Letters* **2010**, *1*, (1), 450-456.
[53] Q. Zheng, H. Kang, J. Yun, J. Lee, J. H. Park, S. Baik, Hierarchical Construction of Self-Standing Anodized Titania Nanotube Arrays and Nanoparticles for Efficient and Cost-Effective Front-Illuminated Dye-Sensitized Solar Cells. *ACS Nano* **2011**, *5*, (6), 5088-5093.

Submitted: April 4, 2018
Accepted: June 19, 2018